THE JOURNAL OF PHYSICAL CHEMISTRY C

Article

Cite This: J. Phys. Chem. C 2018, 122, 1688−1698

pubs.acs.org/JPCC

Effects of TiO_2 in Low Temperature Propylene Epoxidation Using Gold Catalysts

Zheng Lu,[†] Mar Piernavieja-Hermida,[†] C. Heath Turner,[‡] Zili Wu,[§] and Yu Lei*[,†]

[†]Department of Chemical and Materials Engineering, University of Alabama in Huntsville, Huntsville, Alabama 35899, United States

[‡]Department of Chemical and Biological Engineering, University of Alabama, Tuscaloosa, Alabama 35487, United States

[§]Chemical Science Division and Center for Nanophase Materials Sciences, Oak Ridge National Laboratory, Oak Ridge, Tennessee 37831, United States

Supporting Information

ABSTRACT: Propylene epoxidation with molecular oxygen has been proposed as a green and alternative process to produce propylene oxide (PO). In order to develop catalysts with high selectivity, high conversion, and long stability for the direct propylene epoxidation with molecular oxygen, understanding of catalyst structure and reactivity relationships is needed. Here, we combined atomic layer deposition and deposition precipitation to synthesize series of well-defined Au-based catalysts to study the catalyst structure and reactivity relationships for propylene epoxidation at 373 K. We showed that by decorating TiO_2 on gold surface the inverse $TiO_2/Au/SiO_2$ catalysts maintained ∼90% selectivity to PO regardless of the weight loading of the TiO_2. The inverse $TiO_2/Au/SiO_2$ catalysts exhibited improved regeneration compared to $Au/TiO_2/SiO_2$. The inverse $TiO_2/Au/SiO_2$ catalysts can be regenerated in 10% oxygen at 373 K, while the $Au/TiO_2/SiO_2$ catalysts failed to regenerate at as high as 473 K. Combined characterizations of the Au-based catalysts by X-ray absorption spectroscopy, scanning transmission electron microscopy, and UV−vis spectroscopy suggested that the unique selectivity and regeneration of $TiO_2/Au/SiO_2$ are derived from the site-isolated Ti sites on Au surface and Au−SiO_2 interfaces which are critical to achieve high PO selectivity and generate only coke-like species with high oxygen content. The high oxygen content coke-like species can therefore be easily removed. These results indicate that inverse $TiO_2/Au/SiO_2$ catalyst represents a system capable of realizing sustainable gas phase propylene epoxidation with molecular oxygen at low temperature.

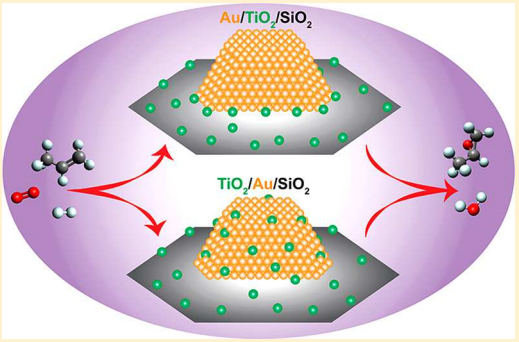

1. INTRODUCTION

Propylene oxide (C_3H_6O, PO) is a chemical intermediate of great value for the production of many useful materials, including polyol, propylene glycol, and glycol ethers.[1] Current industrial PO production such as chlorohydrin and hydroperoxide processes generates chlorinated or peroxycarboxylic byproducts that pose environmental issues. Direct epoxidation of propylene to propylene oxide with oxygen (O_2) represents an alternative, clean, and potentially more efficient route.[2−7] Haruta and co-workers first discovered that nanometer-sized gold clusters on TiO_2 are active and highly selective for the direct epoxidation of propylene with O_2.[2,8,9] It was proposed that when molecular propylene, hydrogen, and oxygen were co-fed, peroxide species could be formed on the surface of gold and subsequently oxidize propylene that adsorbed on TiO_2 sites to propylene oxide. It was later realized that small gold nanoparticles (<5 nm) and isolated Ti active sites are necessary for achieving high activity and selectivity toward propylene oxide. Propylene molecules that adsorb on adjacent Ti sites could lead to formation of unwanted byproducts such as CO_2. For this reason, gold nanoparticles supported by titanium silicalite (Au/TS-1) are the most studied catalysts for the propylene epoxidation reaction as Ti sites are highly isolated in TS-1.[7,10−13] Despite studies over the past decades, the propylene epoxidation reaction still comes short in propylene conversion, catalyst stability, and hydrogen efficiency, and therefore, there is a need to build precise structure−performance relationship for Au-based catalysts for propylene epoxidation reaction and design new catalysts based on this relationship.

In precious metal catalysts, metal surfaces are generally considered as the active sites where catalytic reactions take place. A loss of catalytic activity sometimes results from the strong metal support interaction (SMSI) in which the metal surface active sites gradually become covered by the metal oxide support. However, it has been found that a thin oxide film grown on a metal can exhibit much higher catalytic activity than the metal substrate under the same reaction conditions,[14,15] where a 5 Å FeO(111) film grown on Pt(111) is active for CO oxidation by O_2 at 450 K, a temperature far below that at which Pt(111) itself is active. In a combined experimental and theoretical study, inverse $CeO_2/Au(111)$ catalyst is also found

Received: November 4, 2017
Revised: December 21, 2017
Published: December 21, 2017

DOI: 10.1021/acs.jpcc.7b10902
J. Phys. Chem. C 2018, 122, 1688−1698

to be highly efficient for water gas shift reaction.[16] Thin metal oxide films often exhibit dramatically different chemical and physical properties compared to their bulk counterparts. In particular, if the oxide film is only a few angstroms thick and supported by a metal substrate, the underlying metal substrate often further affects the oxide film properties through charge transfer.[17−20] The concept of the "electronic theory of catalysts" for tuning catalytic activity by the thickness and structure of oxide over metal surface was first developed in the 1950s.[21] Despite the above studies, due to a lack of precise synthesis methods to control the thickness and coverage of the ultrathin (a few nanometers) oxide film overcoat for practical catalyst, the inverse catalyst studies are mostly carried out in surface science studies.

Atomic layer deposition (ALD) is a thin film coating technique commercially used in the microelectronic industry.[22,23] Per the international technology roadmap for semiconductors, the sub-10 nm sized transistor is expected be in commercial mass production by 2018. This trend is expected to be further enhanced by 5 nm sized transistor technology by 2020. It seems that the two disparate industries, namely, semiconductor manufacturing and heterogeneous catalysis, have gradually converged to the same length scale. The high-κ/metal gate materials deposited by ALD play an important role in minimizing the ever smaller dimension of the modern process nodes. ALD's capability to tailor nanomaterials at the atomic scale makes it a promising, alternative method to design and prepare well-defined nanocatalysts.[24−27] ALD has since been utilized to synthesize nanostructured catalysts such as single atom catalysts,[28,29] inverse oxide/metal catalysts,[30−33] bimetallic catalysts,[34−36] and functionalized zeolites.[37−39]

In this work, we carefully alter the TiO_2 ALD cycles and their sequence on Au-based catalysts for the propylene epoxidation reaction. The resulting TiO_2 decorated catalysts provide a well-defined system for studying the effects of TiO_2 geometry and loading on the stability and regeneration ability of the Au-based catalysts, as well as the activity and selectivity of the propylene epoxidation at temperatures as low as 373 K.

2. EXPERIMENTAL SECTION

2.1. Catalyst Synthesis. The composition and structure of the catalysts were carefully designed and tuned by adjusting the sequence of Au and TiO_2 deposited on silica gel. We categorize these catalysts as Au/*n*cTiO_2/SiO_2 or inverse *n*cTiO_2/Au/SiO_2 when TiO_2 or gold was first deposited, respectively. The italic *n* represents the number of TiO_2 ALD cycles.

2.1.1. Synthesis of Au/ncTiO$_2$/SiO$_2$ Catalysts. The Silicycle S10040M SiO_2 with a surface area of ∼100 m^2/g was used as the support. TiO_2 ALD was performed in a viscous flow benchtop reactor (Gemstar-6, Arradiance). Ultrahigh purity N_2 (Airgas, 99.999%) was used as carrier gas and further purified using a Supelco gas purifier (Sigma-Aldrich) before entering the reactor. 500 mg of SiO_2 was uniformly spread onto a stainless steel tray with a mesh cover on top of it. The mesh can prevent the spill of the samples but still provides efficient diffusion of the ALD precursors and product gases in and out of the tray. The time sequence for one cycle ALD can be expressed as t_1−t_2−t_3−t_4, where t_1 and t_3 correspond to the exposure times of the two precursors, and t_2 and t_4 are the nitrogen purge times between two precursors. The TiO_2 was deposited on high surface area SiO_2 gel at a temperature of 473 K using alternating exposure to titanium isopropoxide (TTIP, Sigma-Aldrich, 99.999%) and deionized water, with a time sequence of 25−200−3.75−200 s.[40] The TTIP was stored in a sealed stainless steel bottle at 353 K to provide sufficient vapor pressure. Four samples were prepared using 1, 3, 5, and 10 cycles of TiO_2 ALD over SiO_2. The deposition of gold on TiO_2 ALD modified SiO_2 supports was carried out by means of deposition precipitation (DP).[7] Approximately 0.2 g of $HAuCl_4{\cdot}3H_2O$ (Sigma-Aldrich, 99.99%) was added to 100 mL of deionized water, followed by the addition of 1 g of support. NaOH (1 mol/L) was dropwise added to the solution to keep the pH at ∼7 for 2 h. The solid portion was separated from the solution and washed with 50 mL of deionized water, separated again, and finally dried in air at room temperature overnight.

2.1.2. Synthesis of ncTiO$_2$/Au/SiO$_2$ Catalysts. The precursor $Au(en)_2Cl_3$ was synthesized by slowly adding 0.9 mL of ethylenediamine (en, Sigma-Aldrich, 99.5%) to an aqueous solution of $HAuCl_4{\cdot}3H_2O$ (2.0 g in 20.0 mL of H_2O) until a transparent brown solution was formed.[41] The transparent brown solution was stirred for 30 min. Subsequently, 140.0 mL of ethanol was added. A precipitation was immediately produced. The solution was stirred for another 40 min. The final product was filtered, washed by 160 mL ethanol, and dried overnight in oven at 313 K.

An amount of 0.27 g of $Au(en)_2Cl_3$ was dissolved in 150 mL of H_2O. The pH value of the solution was adjusted to 10.0 by the addition of the NaOH (1 mol/L) solution. Subsequently, 5.25 g of the silica gel was added. The pH value of the solution decreased immediately, and then the pH value was adjusted to 10.0 by addition of the NaOH solution. The mixed solution was stirred for 2 h. The solid was separated from the solution and washed by 50 mL of deionized water, separated again, and finally dried in vacuum oven for 5 h.

TiO_2 ALD was performed in the same way mentioned before. Four samples were prepared using 1, 3, 5, and 10 TiO_2 ALD cycles over Au/SiO_2.

2.2. Characterization. In situ quartz crystal microbalance (QCM) measurements were carried out under ALD conditions in real time to establish the TiO_2 ALD recipe and to understand the surface chemistry. The QCM system contains a Maxtek BSH-150 bakeable sensor, AT-cut quartz sensor crystals (Colorado Crystal Corporation), and a Maxtek TM400 film thickness monitor. Once the TiO_2 ALD recipe was established, various ALD cycles of TiO_2 thin films were deposited on Si(100) wafers. The thickness of the TiO_2 thin films was measured using a J. A. Woollam alpha-SE variable angle spectroscopic ellipsometer (VASE). The data were obtained over a wavelength of 380−900 nm and an incidence angle of 70°. The time sequence for operating one ALD cycle of TiO_2 on planar quartz sensor crystals and Si(100) wafers is 1−5−1−5 s.

Scanning electron microscopy (SEM) measurements were carried out using a benchtop microscope (Hitachi TM-1000). The high angle annular dark field scanning transmission electron microscopy (HAADF-STEM) imaging was performed using a FEI Tecnai F-20 transmission electron microscope equipped with a 200 keV thermal Schottky field emission gun. The size histogram of gold nanoparticles was determined by measuring the diameter of more than 250 particles for each catalyst. X-ray diffraction (XRD) measurements were carried out using Rigaku MiniFlex 600 powder X-ray diffractometer using Cu Kα radiation operated at 40 kV and 15 mA; 2θ data from 2° to 90° were obtained at a scanning speed of 0.5°/min. The Brunauer−Emmett−Teller (BET) surface area was

DOI: 10.1021/acs.jpcc.7b10902
J. Phys. Chem. C 2018, 122, 1688−1698

measured via nitrogen adsorption at 77 K by Micromeritics Gemini 275 system. The UV−vis diffuse reflectance spectra (DRS) of the fresh, spent, and regenerated samples were obtained using a Cary 5000 UV/vis spectrophotometer equipped with a praying mantis kit at room temperature. The amount of gold deposited on the support was determined by inductively coupled plasma mass spectrometry (ICP-MS).

Fourier transform infrared (FTIR) spectroscopy measurements were performed using PerkinElmer FT-IR Spectrum Two spectrophotometer with diamond attenuated total reflectance (ATR) attachment. With an average of eight repetitious scans, the scanning was conducted from 4000 to 400 cm^{-1}. Prior to measurement, the samples were placed evenly and pressed to contact with the ATR crystal to obtain adequate band intensities. From the pressure readout, the same force was applied to acquire quantitative analysis for SiO_2 concentration.

X-ray absorption spectroscopy (XAS) measurements, including extended X-ray absorption fine structure spectroscopy (EXAFS) and X-ray absorption near edge structure spectroscopy (XANES), were conducted at the Au L_3 edge (~11 919 eV) at beamline 10-BM of the Materials Research Collaborative Access Team (MRCAT) at the Advanced Photon Source (APS) at Argonne National Laboratory. The XAS spectra were recorded in the transmission mode. The samples were pressed into a cylindrical holder which can hold six samples simultaneously. The loading of the sample was optimized to achieve a step height of 1. In a typical measurement, the catalyst samples were first fully reduced in 50 mL/min 3.5% H_2 in helium at 523 K for 30 min and subsequently cooled to room temperature in ultrahigh purity helium. EXAFS regime data fittings were performed using WINXAS 3.1. A single shell model fit of the EXAFS data was obtained between k = 3.0−12.0 $Å^{-1}$ and r = 1.6−3.5 Å, respectively.

2.3. Measurement of Catalytic Activity. The catalytic reaction for gas-phase propylene epoxidation was carried out in a quartz tubular reactor with a diameter of 10 mm at normal pressure. The quartz tube reactor was placed within a furnace using approximately 0.15 g of catalyst of 60−80 mesh size. Approximately 1.5 g of quartz sand of 25−35 mesh size was used to dilute the catalyst to improve the temperature uniformity. A blank experiment was performed under the same reaction conditions using only the quartz sand. A thermocouple was attached on the quartz tube wall to directly measure the reaction temperature. The reactant mixture consisted of 10/10/10/70 vol % of hydrogen (Airgas, 99.999%), oxygen (Airgas, 99.999%), propylene (Matheson, 99.9%), and argon (Airgas, 99.999%), with a total flow of 35 mL/min equivalent to a gas hourly space velocity (GHSV) of 14 000 mL h^{-1} g^{-1}_{cat}. Without any pretreatment of the catalyst, the epoxidation reaction was carried out at 373 ± 2 K, which was reached by a temperature ramp rate of 1.5 K/min. The effluent line was wrapped with heating tape and heated to above 80 °C to prevent condensation of all the byproducts.

The experimental conditions for kinetic studies are listed in Table S1 in Supporting Information. To extract the oxygen order, the oxygen concentration was changed solely at 453 K. The changes in propylene and hydrogen concentrations were used to extract propylene and hydrogen orders. Since the reaction order is independent with temperature, the same reaction order for each reactant was applied to derive the reaction rate constant k at 413, 433, and 453 K.

When hydrogen peroxide was used as a reactant, a syringe pump equipped with a borosilicate syringe through a Teflon tube was used to directly introduce H_2O_2 (30 wt %, Sigma-Aldrich, containing stabilizer) into the reactor. To minimize the H_2O_2 decomposition, the syringe and Teflon tubing were wrapped with aluminum foil and their length was minimized. The partial pressure of H_2O_2 could be adjusted by changing the pumping speed. A bed of quartz wool around 4 cm was placed above the catalyst bed where H_2O_2 fully evaporated. On the basis of the assumption that H_2O_2 can be fully decomposed to H_2O and O_2 through the heated stainless steel reactor, a blank run with only H_2O_2 in argon was performed to measure the weight percentage of the H_2O_2 solution. The H_2O_2 weight percentage calculated from O_2 in the effluent is around 33 ± 2%, which is similar to the specification.

The concentration of the reactants and products was measured by an online gas chromatograph (GC, Agilent 5890) equipped with a flame ionization detector (FID) and a thermal conductivity detector (TCD). Oxygen, hydrogen, and propylene were separated using Carboxen-1010 PLOT capillary column (length 30 m; i.d. 0.53 mm) and analyzed via TCD, while propylene oxide, ethanal, acetone, propanal, and acrolein were separated using a RT-U-BOND column (length 30 m; i.d. 0.53 mm) and analyzed via FID. Carbon monoxide (CO) and carbon dioxide (CO_2) were not detected under the reaction conditions used in this study. The propylene conversion and selectivity were calculated directly as follows:

$$\text{conversion} = \frac{\text{moles of } (C_3\text{-oxygenates} + (2/3)\text{ethanal})}{\text{moles of propylene in the feed}} \quad (1)$$

$$\text{PO selectivity} = \frac{\text{moles of PO}}{\text{moles of } (C_3\text{-oxygenates} + (2/3)\text{ethanal} + CO_2/3)} \quad (2)$$

3. RESULTS AND DISCUSSION

3.1. TiO_2 Atomic Layer Deposition. For the purpose of precisely controlling the loading of TiO_2 using ALD, the growth rate of TiO_2 ALD was carefully studied using an in situ quartz crystal microbalance (QCM) housed inside the ALD chamber and was later confirmed using ex situ spectroscopic ellipsometry measurements. The in situ QCM results in Figure 1a show a mass gain of 0.06 $\mu g/cm^2$ per TiO_2 ALD cycle, equivalent to a growth rate of 0.3 Å per TiO_2 ALD cycle when TTIP and H_2O were used as the reactants at 473 K. The linear growth rate indicates that the ALD growth indeed follows a surface self-limiting nature. An expanded view of the mass gain is illustrated in Figure 1b. The surface received +0.08 $\mu g/cm^2$ (chemisorption of $-Ti(OCH(CH_3)_2)_2$ ligands) and −0.04 $\mu g/cm^2$ mass gain $-OCH(CH_3)_2$ ligands replaced by hydroxyl groups) during TTIP and H_2O exposure, respectively, which is consistent with the literature.[40,42] A series of TiO_2 thin films, using 50, 100, 200, and 300 cycles of TiO_2 ALD, respectively, were prepared on clean Si(100) wafers. The thickness of TiO_2 increases linearly as a function of TiO_2 ALD cycles with a growth rate of 0.3 Å as determined by ex situ spectroscopic ellipsometry in Figure 1c. Both QCM and ellipsometry results are consistent with each other.

Due to its unique feature of self-limiting surface reactions, the growth rate obtained from the wafers was used to estimate

DOI: 10.1021/acs.jpcc.7b10902
J. Phys. Chem. C 2018, 122, 1688−1698

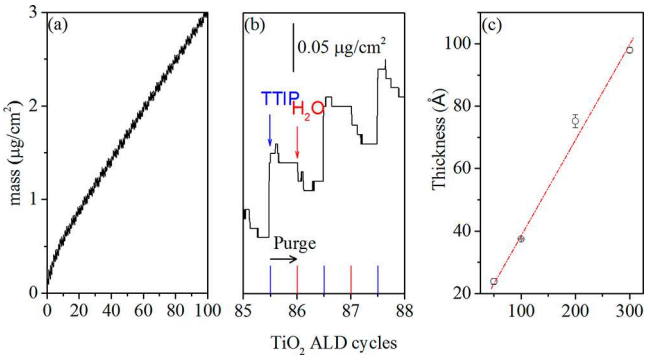

Figure 1. In situ QCM studies of TiO_2 ALD at 473 K for (a) the first 100 cycles and (b) magnified growth rate (blue line, TTIP pulse; red line, H_2O pulse). (c) Growth rate of TiO_2 ALD at 473 K determined by ex situ spectroscopic ellipsometry.

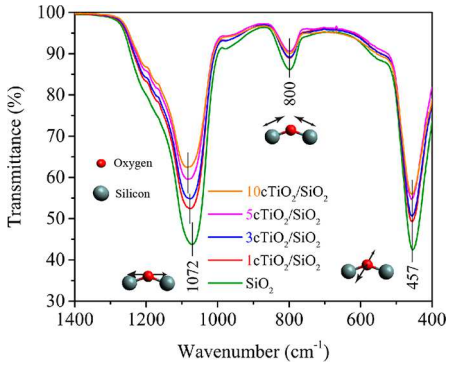

Figure 2. ATR-FTIR transmittance spectra of SiO_2 (green), $1cTiO_2/SiO_2$ (red), $3cTiO_2/SiO_2$ (blue), $5cTiO_2/SiO_2$ (pink), and $10cTiO_2/SiO_2$ (orange).

the TiO_2 surface coverage on the SiO_2 gel support using eqs 3 and 4. The SEM image of the bare SiO_2 gel is shown in Figure S1. The coverage θ is obtained from the following equations,

$$\theta = \frac{d}{\hat{d}} \tag{3}$$

$$\hat{d} = \sqrt[3]{\frac{M}{\rho N}} \tag{4}$$

where d is the deposited TiO_2 thickness, $\hat{d}$ is TiO_2 monolayer thickness in nm, M is the molar mass of TiO_2 (79.87 g/mol), ρ is the density of TiO_2 (4.23×10^{-21} g/nm^3), and N is the number of atoms per mole (6.02×10^{23}/mol). In this work, catalysts were coated by 1, 3, 5, and 10 TiO_2 ALD cycles, respectively. Their estimated thickness, coverage, and weight loading are shown in Table 1. If we assume that one ALD cycle

Table 1. Estimated Thickness, Coverage, and Weight Loading after TiO_2 ALD Treatment[a]

cycle number of TiO_2 ALD	estimated thickness (Å)	coverage θ (%)	estimated TiO_2 loading (wt %)
1	0.3	9.7	1.3
3	0.9	29.1	3.8
5	1.6	48.4	6.4
10	3.1	96.9	12.7

[a]The monolayer thickness $\hat{d}$ is equal to 3.2 Å.

of TiO_2 is site-isolated and homogeneously dispersed on SiO_2 surface, the intermolecular distance is estimated to be ~13.6 Å. BET surface area measurements were carried out before and after 10 cycles of TiO_2 ALD. The N_2 adsorption−desorption isotherms exhibit typical H4-type hysteresis, indicating the presence of mesopores. The ALD coating did not alter the surface area or pore volume or pore size of the SiO_2 support (see Figure S2).

Figure 2 is the FTIR spectra of SiO_2 modified by different ALD cycles of TiO_2. The spectra exhibited three dominant features, and these are assigned as the low frequency band centered at 457 cm^{-1} formed by the rocking motions of the oxygen atoms perpendicular to the Si−O−Si plane; the intermediate frequency band centered at 800 cm^{-1} is due to the symmetrical stretching of the oxygen atoms along the line bisecting the axis formed by the Si−O−Si; the high frequency band centered at 1072 cm^{-1} is attributed to the antisymmetric stretching of the oxygen atoms along the direction parallel to Si−Si.[43] The intensity of those dominant peaks decreased as TiO_2 ALD cycles increased, which corresponded to the increase of TiO_2 loading. In addition, the peak position of the Si−O−Si antisymmetric stretching vibration shifted to higher wavenumber (blueshift, from 1072 to 1082 cm^{-1}) with the increase of TiO_2 incorporation, which implies that the Si−O−Si bond angle increased and/or the Si−O bond length decreased.[44]

3.2. Characterizations. Figure 3 shows the STEM images of the as-prepared samples where homogeneously dispersed gold nanoparticles on the titanium coated the SiO_2 support. Unfortunately, it is unlikely that STEM can provide useful information on TiO_2, since the catalyst support SiO_2 gel is a high surface area porous material, which is considered as not well-defined for atomic resolution STEM. In addition, the low loading and low z-number of Ti make it more difficult to be distinguished from the SiO_2 background. The average diameter of the as-prepared gold nanoparticles is 3.6 ± 0.6 nm and 4.1 ± 0.5 nm for the as-prepared $Au/3cTiO_2/SiO_2$ and $Au/10cTiO_2/SiO_2$ catalysts, respectively. Au nanoparticles appear as bright dots on the TiO_2 coated SiO_2 support. ICP-MS measurements showed that the amounts of gold were ~0.05 wt % and ~0.7 wt % for $Au/ncTiO_2/SiO_2$ series and $ncTiO_2/Au/SiO_2$ series, respectively.

Figure 4 shows the XRD patterns for the as-prepared $10cTiO_2/SiO_2$, the as-prepared $Au/10cTiO_2/SiO_2$, and the $Au/10cTiO_2/SiO_2$ calcined at 600 °C for 2 h. The broad peaks at 2θ range from 20° to 30°, and they are representative peaks for an amorphous SiO_2 support. Neither TiO_2 nor Au features were clearly observed in the XRD patterns of the as-prepared $Au/10cTiO_2/SiO_2$. The missing features seem to suggest that both TiO_2 and Au are highly dispersed on the SiO_2 support, which is desired for highly active propylene epoxidation catalysts. The $Au/10cTiO_2/SiO_2$ catalyst was calcined in air at 600 °C for 2 h to artificially increase the gold particle diameter. Indeed, the calcined $Au/10cTiO_2/SiO_2$ catalysts show sharp diffraction peaks that are consistent with the face-centered cubic (fcc) gold structure.

To understand the impact of TiO_2 loading and location on the morphological and electronic structure of the Au catalysts, Au L_3 XAS measurements were carried out. The Au catalysts were in a metallic oxidation state (see XANES spectra in Figure S3). Regardless the location of TiO_2, Fourier transform EXAFS spectra of $Au/1cTiO_2/SiO_2$ and $1cTiO_2/Au/SiO_2$ are very similar, as shown in Figure 5a. Both spectra showed peaks in the magnitude of the Fourier transform for the first shell Au−

DOI: 10.1021/acs.jpcc.7b10902
J. Phys. Chem. C 2018, 122, 1688−1698

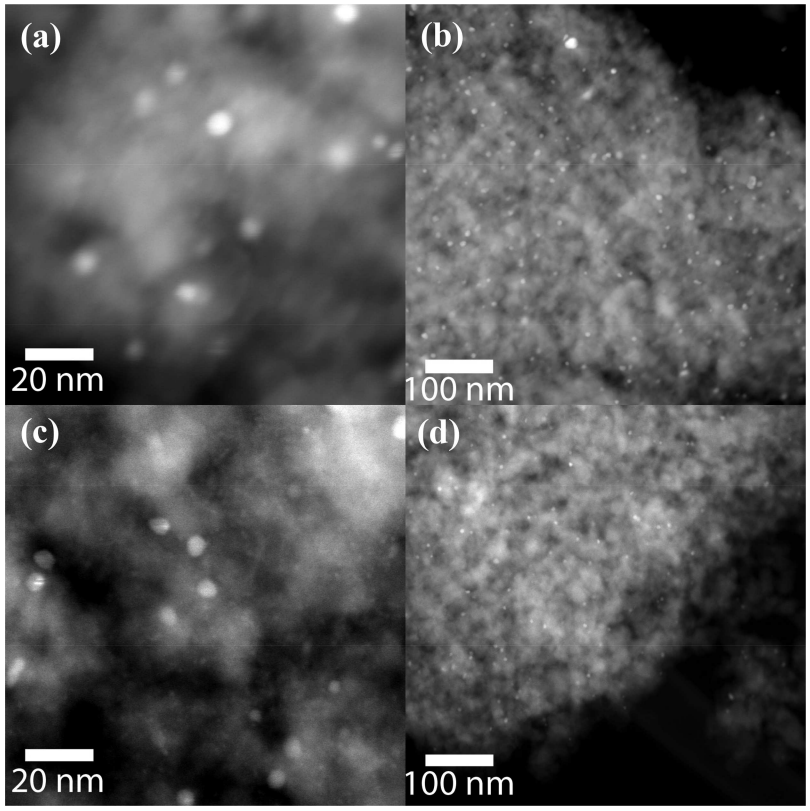

Figure 3. STEM images of the as-prepared Au/3cTiO$_2$/SiO$_2$ (a, b) and Au/10cTiO$_2$/SiO$_2$ (c, d) catalysts.

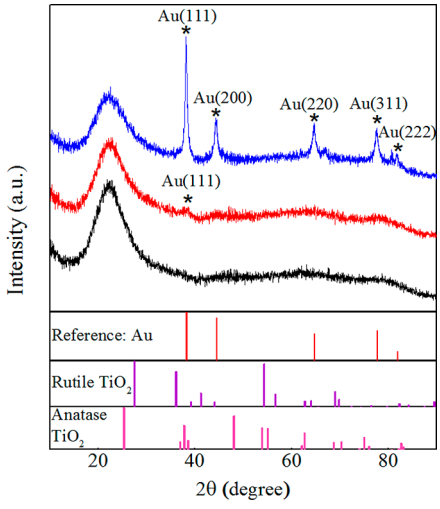

Figure 4. XRD patterns for 10cTiO$_2$/SiO$_2$ (black), Au/10cTiO$_2$/SiO$_2$ (red), and Au/10cTiO$_2$/SiO$_2$ calcined at 600 °C for 2 h (blue).

Au at about 2.3 and 3.0 Å and a shoulder peak at about 2.0 Å. Detailed EXAFS first shell fittings are concluded in Table 2, and the fitting quality is shown in Figures S4 and S5. The Au−Au bond distance of the gold nanoparticles is about 2.81−2.85 Å, slightly contracted from the Au−Au bond distance of 2.88 Å in a bulk Au. A contracted bond distance is widely observed in precious nanoparticles and is caused by the contraction of the undercoordinated surface atoms to increase the coordination numbers of the surface atoms.[45,46]

The Au−Au coordination numbers are well below their bulk value of 12 which is expected for a bulk fcc structure, indicating that the gold is in the form of small nanoparticles. Diameter of

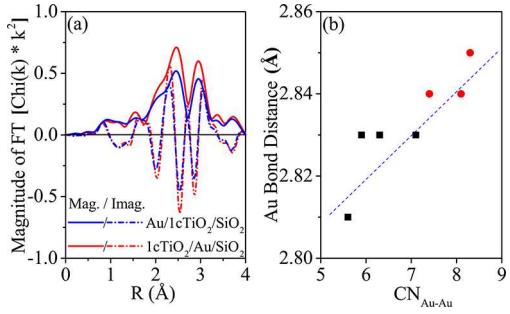

Figure 5. (a) Fourier transform of EXAFS. (b) Correlation between the CN$_{Au-Au}$ and Au−Au bond distance for a series of catalysts Au/*n*cTiO$_2$/SiO$_2$ (black square) and *n*cTiO$_2$/Au/SiO$_2$ (red dot).

Table 2. EXAFS Fit Parameters for Au−Au Scatterers[a]

sample	CN$_{Au-Au}$	*R* (Å)	DWF (×10^{-3})	E_0 (eV)	est dia (nm)
Au/*n*cTiO$_2$/SiO$_2$					
Au/1cTiO$_2$/SiO$_2$	5.9	2.83	0.001	−1.7	1.3
Au/3cTiO$_2$/SiO$_2$	6.3	2.83	0.001	−1.9	1.6
Au/5cTiO$_2$/SiO$_2$	5.6	2.81	0.001	−2.3	1.1
Au/10cTiO$_2$/SiO$_2$	7.1	2.83	0.001	−3.0	2.1
*n*cTiO$_2$/Au/SiO$_2$					
1cTiO$_2$/Au/SiO$_2$	8.1	2.84	0.001	−1.7	2.7
3cTiO$_2$/Au/SiO$_2$	7.4	2.84	0.001	−1.7	2.3
5cTiO$_2$/Au/SiO$_2$	8.3	2.85	0.001	−1.5	2.9

[a] k^2: Δk = 3−12 Å^{-1} and Δr = 1.6−3.5 Å. CN is coordination numbers with error of ±10%. *R* is bond distance with error of ±0.02 Å. DWF is Debye−Waller factor. E_0 is energy shift.

DOI: 10.1021/acs.jpcc.7b10902
J. Phys. Chem. C 2018, 122, 1688−1698

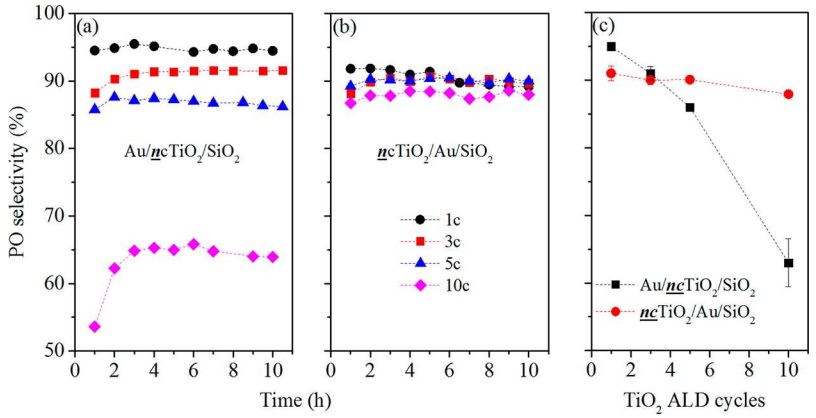

Figure 6. PO selectivity for series of catalysts (a) Au/ncTiO$_2$/SiO$_2$ and (b) ncTiO$_2$/Au/SiO$_2$: n = 1 (black line), n = 3 (red line), n = 5 (blue line), and n = 10 (pink line). (c) Average PO selectivity for series of catalysts Au/ncTiO$_2$/SiO$_2$ (black line) and ncTiO$_2$/Au/SiO$_2$ (red line) under different cycle of TiO$_2$ ALD modification.

the Au nanoparticles can be estimated using their coordination numbers using an empirical equation suggested by Miller and co-workers.[47] The results are listed in Table 2. The Au−Au coordination and interatomic Au−Au bond length exhibit a linear relationship within the range of our study, as shown in Figure 5b. It seems to suggest that the structure of gold is independent of the location of TiO$_2$. The diameters of gold nanoparticles of all the samples are smaller than the STEM results. We ascribed the difference to the low resolution of the conventional STEM that we used. The estimated diameter of Au in the ncTiO$_2$/Au/SiO$_2$ catalysts is slightly larger than the Au/ncTiO$_2$/TiO$_2$ catalysts. The difference in diameter is probably caused by slightly different methods used to prepare Au nanoparticles on TiO$_2$/SiO$_2$ and SiO$_2$ surface, respectively. Due to the mismatch between the isoelectric point of SiO$_2$ (IEP = 2) and pH used to hydrolyze the Au precursors (HAuCl$_4$), Au(en)$_2$Cl$_3$ had to be used to prepare Au nanoparticles on the SiO$_2$ surface.

3.3. Catalyst Performance in Propylene Epoxidation.

3.3.1. PO Selectivity. Table S2 lists the selectivity for all the byproducts. There is no CO or CO$_2$ detected in this study as their concentration is likely below the detection limit of the TCD detector. The PO selectivity decreased with increasing TiO$_2$ ALD cycles for the Au/ncTiO$_2$/SiO$_2$ catalysts as shown in Figure 6. The selectivity to PO decreased from 95% to 63% when the TiO$_2$ ALD cycle increased from 1 to 10 cycles. In the previous propylene epoxidation studies, isolated Ti sites are believed to be critical to obtain high selectivity for propylene epoxidation reaction as the adjacent Ti sites can generate byproducts such as acrolein, propanal, and acetone.[48] Our results are consistent with this observation in the literature. According to previous studies on TiO$_2$ ALD, TTIP precursors react with the surface hydroxyl groups and generate isolated Ti sites in the first cycle. In the subsequent TiO$_2$ ALD cycles, the TTIP precursors will react with both the hydroxyl groups on open Si sites to generate more isolated Ti sites, as well as the hydroxyl groups on the Ti sites to generate adjacent Ti sites. The overall effect is that the isolated sites decrease with increasing TiO$_2$ ALD cycles, leading to decreasing PO selectivity.

Interestingly, the PO selectivity of the ncTiO$_2$/Au/SiO$_2$ catalysts seems to be less affected by TiO$_2$ ALD cycles as shown in Figure 6b. The selectivity to PO decreases slightly from ~91% to ~88% when the TiO$_2$ ALD cycle increases from 1 to 10 cycles, which seems to suggest that the TiO$_2$ deposited on Au remains mostly isolated. It is useful to notice that the TiO$_2$ ALD growth rate also depends on the density of surface active sites, e.g., surface hydroxyl groups in this case. The real growth rate of TiO$_2$ ALD on Au could be significantly lower than TiO$_2$ ALD on SiO$_2$ due to much lower density of surface OH on Au. The low coverage of OH on Au could be helpful to keep the TiO$_2$ site isolated. Surface science studies of the synthesis of TiO$_2$ nanoparticles on Au(111) surface showed that TiO$_2$ forms islands at a coverage as low as 0.05 ML;[49] however, Ti was generated using physical vapor deposition (PVD) on a clean surface without hydroxyl groups. The deposited titanium metal first formed Au−Ti alloys on the surface of Au. TiO$_2$ was subsequently formed by exposing the system to O$_2$. In the case of TiO$_2$ ALD, it is likely that TTIP reacts with the surface hydroxyl groups near Au or at Au/SiO$_2$ interface forming Au−O−Ti bonds which can enhance the thermal stability of the system and help Ti sites to remain isolated. Such increased thermal stability is similar to surface science studies of model Au catalysts on hydroxylated surface.[50] It is known that TiO$_2$ can be formed on Au nanoparticles' surface even with a very small number of TiO$_2$ ALD cycles. For example, it was reported that the CO chemisorption dramatically decreased after depositing five ALD cycles of TiO$_2$ on Au/Al$_2$O$_3$ surface.[51]

3.3.2. PO Formation Rate. In terms for PO formation rate, five ALD cycles of TiO$_2$ seem to offer the highest PO formation rate in both Au/ncTiO$_2$/SiO$_2$ and ncTiO$_2$/Au/SiO$_2$ series, representing the optimal synergic effects between isolated Ti sites and Au. For Au/ncTiO$_2$/SiO$_2$ catalysts (Figure 7a), the PO formation rate increases with increasing number of TiO$_2$ ALD cycles from 1 to 5. We ascribed the increasing PO formation rate to the increasing number of Au and Ti pairs. Accompanied with a significant increase in byproduct selectivity (see Table S2), the PO formation rate dramatically decreased when 10 ALD cycles of TiO$_2$ were used, due to the loss of isolated Ti sites. For ncTiO$_2$/Au/SiO$_2$ series (Figure 7b), TiO$_2$ gradually covers the surface of gold nanoparticles when the TiO$_2$ ALD cycles increase from 1 to 10, leading to an increase of Ti sites and a decrease of Au sites. Three to five ALD cycles of TiO$_2$ on Au nanoparticles seem to provide an optimized balance between Ti and Au sites. Note that Au/SiO$_2$ was also studied as a controlled experiment. No reactivity was observed.

DOI: 10.1021/acs.jpcc.7b10902
J. Phys. Chem. C 2018, 122, 1688−1698

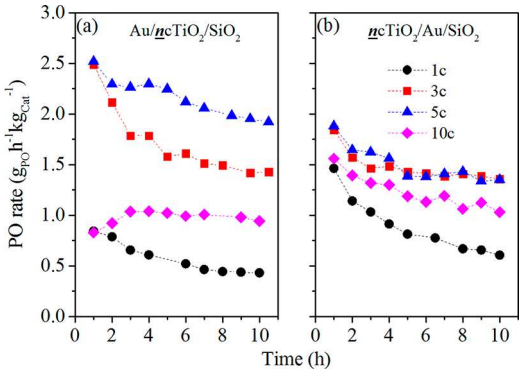

Figure 7. PO formation rate for series of catalysts (a) Au/*n*cTiO$_2$/SiO$_2$ and (b) *n*cTiO$_2$/Au/SiO$_2$: n = 1 (black line), n = 3 (red line), n = 5 (blue line), and n = 10 (pink line).

3.3.3. Deactivation and Regeneration. Unfortunately, the Au-based catalysts studied in this work all suffered from a certain degree of deactivation when they were evaluated at 373 K. The time-on-stream stability is shown in Figure 8. After being tested for 10 h under reaction conditions, Au/1cTiO$_2$/SiO$_2$ and 1cTiO$_2$/Au/SiO$_2$ catalysts deactivated by 48.6% and 54.8%, respectively. In an attempt to regenerate both catalysts, the spent catalysts were regenerated in 10% O$_2$ at 373 K for 2 h. The treatment successfully regenerated the overcoated 1cTiO$_2$/Au/SiO$_2$ to its initial performance but failed to regenerate Au/1cTiO$_2$/SiO$_2$. An additional attempt to regenerate Au/1cTiO$_2$/SiO$_2$ catalyst at a higher temperature (473 K) was also unsuccessful. To confirm the above observations, repeated experiments were performed to test and regenerate both Au/1cTiO$_2$/SiO$_2$ and 1cTiO$_2$/Au/SiO$_2$ catalysts. Similar phenomena were observed.

There are three possible reasons for gold-based catalysts deactivation in propylene epoxidation, namely, sintering of gold nanoparticles, carbon deposition (coking) on the active sites, and the rearrangement of active TiO$_2$ sites. Figure 9 shows the STEM images of the spent catalysts Au/3cTiO$_2$/SiO$_2$ and Au/10cTiO$_2$/SiO$_2$. The average size of observable gold nanoparticles was 2.9 and 4.0 nm, respectively, similar to their diameter before the catalyst evaluation. XRD patterns were also measured on the spent catalysts immediately after the catalyst evaluation. The XRD patterns of the spent catalysts (data not shown) are similar to those of the as-prepared catalysts where no peaks ascribed to fcc Au was observed, indicating small gold nanoparticles. In a control experiment, hydrogen peroxide (H_2O_2) and propylene (1:1 molar ratio) were co-fed to evaluate the 1cTiO$_2$/SiO$_2$ catalyst. The catalyst 1cTiO$_2$/SiO$_2$ deactivated by 52.9%. Treatment in 10% O$_2$ at 373 K for 2 h did not regenerate the catalyst, suggesting that the deactivation is probably due to factors other than sintering of gold nanoparticles.

Another possible reason for catalyst deactivation is the TiO$_2$ rearrangement during reaction. This rearrangement can be reflected by the change of the Ti coordination numbers which was investigated using UV−vis DRS spectroscopy. The absorption spectra were recorded for fresh, deactivated, and regenerated catalysts as shown in Figure 10 for Au/1cTiO$_2$/SiO$_2$ and 1cTiO$_2$/Au/SiO$_2$. The spectra in each of those three catalysts showed the same trend which excludes the change in TiO$_2$ and gold geometry as one of the reasons for catalysts deactivation and regeneration. The strong absorptions at 200−220 nm are assigned to isolated tetrahedral Ti in the framework.[52] The band around 230 and 275 nm are attributed to the presence of Ti in 5-fold and 6-fold coordination,[53] respectively, while that at ∼305 nm corresponds to anatase TiO$_2$.[54] The spectra show an absorption in the visible range between 500 and 600 nm assigned to the localized surface plasmon resonance of Au nanoparticles.[55]

As a result, it seems that the possible reason for the deactivation is the residual carbon blocking the catalyst active sites. Coke-like species were previously observed using in situ Raman spectroscopy[56] and IR spectroscopy,[57,58] respectively. These species have been assigned as strongly adsorbed oligomerization or polymerization of propylene or propylene oxide,[59] bidentate propoxy species,[57] and carbonates/carboxylates.[48] The true identity of the coke-like species is yet to be determined. One possible explanation is that the coke-like organic species generated by the 1cTiO$_2$/Au/SiO$_2$ contain a relatively high oxygen content and are easy to be burned off, as compared to the possible low-oxygen content coke species produced by Au/1cTiO$_2$/SiO$_2$.

3.3.4. Kinetic Studies. Kinetic studies of Au/1cTiO$_2$/SiO$_2$ and 1cTiO$_2$/Au/SiO$_2$ catalysts were performed by varying the concentration of the reactants and reaction temperatures. The detailed experimental conditions listed in Table S1 follow those

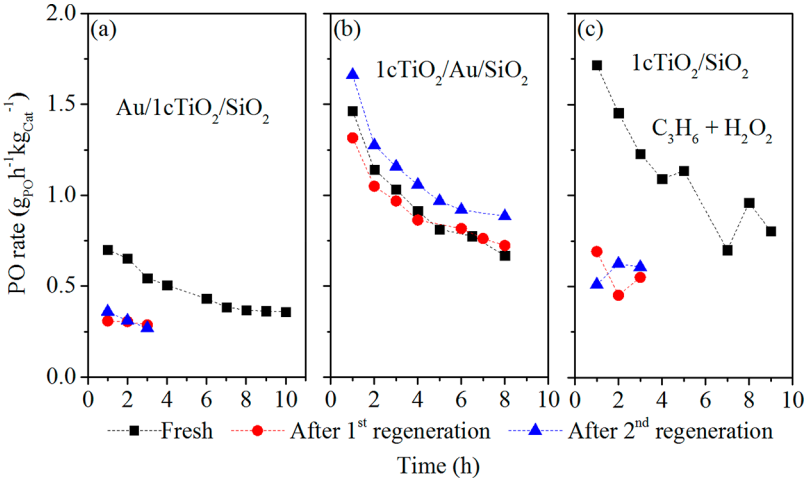

Figure 8. PO formation rate for catalyst (a) Au/1cTiO$_2$/SiO$_2$, (b) 1cTiO$_2$/Au/SiO$_2$, and (c) 1cTiO$_2$/SiO$_2$.

DOI: 10.1021/acs.jpcc.7b10902
J. Phys. Chem. C 2018, 122, 1688−1698

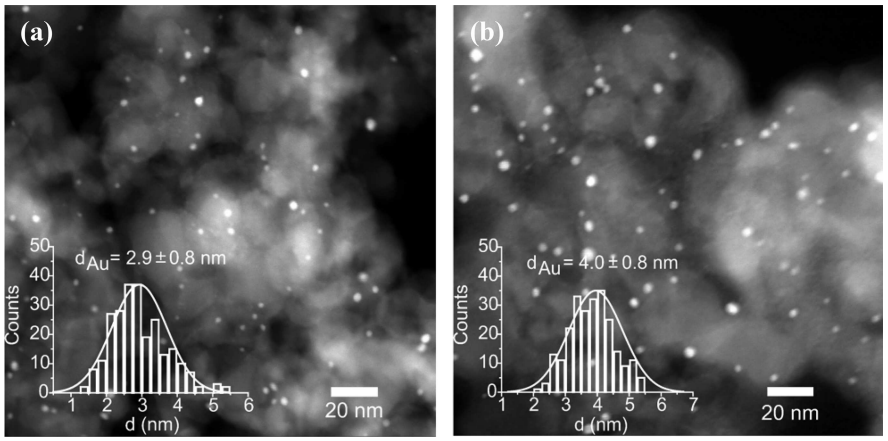

Figure 9. STEM images of spent catalysts (a) Au/3cTiO$_2$/SiO$_2$ and (b) Au/10cTiO$_2$/SiO$_2$. The insets show the gold nanoparticle size distributions.

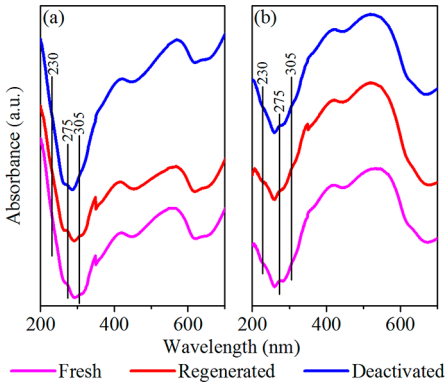

Figure 10. UV−vis DR spectra for samples (a) Au/1cTiO$_2$/SiO$_2$ and (b) 1cTiO$_2$/Au/SiO$_2$.

used by Taylor et al.[60] Twenty-three sets of experiments were carried out to determine the reaction order and rate constant for each catalysts. The experimental results are presented in Tables S3 and S4. Unlike the experiments operated at low temperature (373 K), little deactivation was observed during the kinetic measurements performed above 413 K, suggesting that the carbon species were removed by oxygen under reaction conditions. From the previous studies, PO has strong interaction with the catalyst surface and is considered to have negative impact on catalyst performance due to active sites blocking.[61] Therefore, PO concentration would be expected in powder rate law. Because of the relatively low propylene conversion, PO concentration is approximately 2 orders of magnitude less than the concentration of each reactant. Moreover, no obvious catalyst deactivation is observed, which indicates that interaction between PO and catalyst surface could be ignored. Hence, it is reasonable to neglect the formed PO concentration in the power rate law. Those two catalysts were fit individually using the linear regression features. To keep a linear model, ln(k) rather than k was fitted. The power rate law converted to the following equation,

$$\ln(r_{PO}) = \ln(k) + \alpha \ln[H_2] + \beta \ln[O_2] + \gamma \ln[C_3H_6] \quad (5)$$

The overall data fitting is shown in Figure S6 where all the data points overlap or are close to the parity lines. Figure S7 shows the percent residual randomly distributed around the zero lines within ±10%. The derived fitting parameters were shown in Table 3. For catalyst Au/1cTiO$_2$/SiO$_2$, PO formation rate was found to be most dependent on hydrogen concentration, whereas oxygen has the highest effect on PO rate for catalyst 1cTiO$_2$/Au/SiO$_2$. The rate law of propylene epoxidation using Au/1cTiO$_2$/SiO$_2$ and 1cTiO$_2$/Au/SiO$_2$ catalysts are similar to what Delgass and co-workers observed on Au/TS-1 catalysts where they obtained a rate law $r_{PO} = k[H_2]^{0.60}[O_2]^{0.31}[C_3H_6]^{0.18}$.[60] The apparent activation energy is derived based on the Arrhenius plot shown in Figure 11. The

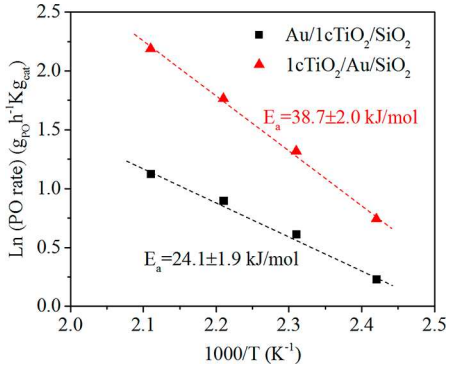

Figure 11. Arrhenius plot for propylene epoxidation using Au/1cTiO$_2$/SiO$_2$ and 1cTiO$_2$/Au/SiO$_2$ catalysts, respectively. Reaction conditions: 10% O_2, 10% H_2, and 10% C_3H_6 in Ar.

activation energy E_a for Au/1cTiO$_2$/SiO$_2$ and 1cTiO$_2$/Au/SiO$_2$ catalysts is 24.1 and 38.7 kJ/mol, respectively, comparable to the literature value (25−36 kJ/mol).[62] These results seem to

Table 3. Power Rate Law Parameters Obtained[a]

catalyst	α	β	γ	$k(140)$[b]	$k(160)$[b]	$k(180)$[b]	E_a[c]
Au/1cTiO$_2$/SiO$_2$	0.52	0.33	0.22	14.22	22.55	30.48	24.1 ± 1.9
1cTiO$_2$/Au/SiO$_2$	0.39	0.49	0.26	25.35	46.05	74.71	38.7 ± 2.0

[a] $r_{PO} = k(T)[H_2]^{\alpha}[O_2]^{\beta}[C_3H_6]^{\gamma}$, where $k(T) = Ae^{[(-E_a/(RT)]}$. [b] Unit: $g_{PO}/(h \cdot kg_{cat} \cdot atm^{\alpha+\beta+\gamma})$. [c] Unit: kJ/mol.

DOI: 10.1021/acs.jpcc.7b10902
J. Phys. Chem. C 2018, 122, 1688−1698

suggest that the active sites in ALD modified Au/1cTiO_2/SiO_2 and 1cTiO_2/Au/SiO_2 catalysts are similar to those in Au/TS-1.

4. CONCLUSIONS

We used ALD to carefully synthesize Au/TiO_2/SiO_2 and inverse TiO_2/Au/SiO_2 catalysts used in propylene epoxidation with molecular oxygen to propylene oxide. Our study showed that inverse TiO_2/Au/SiO_2 enabled high PO selectivity (~90%) and easy regeneration at 373 K, results not found in Au/TiO_2/SiO_2. The high PO selectivity independent of TiO_2 ALD cycles indicated that the ALD TiO_2 remained as site-isolated on Au surface and Au−SiO_2 interfaces. Furthermore, combined STEM and UV−vis spectroscopy studies suggested that the deactivation of the gold-based catalysts was due to deposition of coke-like species. The repeated, easy regeneration of the inverse TiO_2/Au/SiO_2 at low temperature is proposed to result from high oxygen content coke-like species that can be removed at low temperature (373 K). It is interesting to note that similar deactivation and failure to regenerate were observed on TiO_2/SiO_2 catalyst used in propylene epoxidation with hydrogen peroxide at 373 K. It is envisioned that a potentially energy efficient, low temperature propylene epoxidation can be achieved by using the inverse TiO_2/Au/SiO_2 catalysts. Kinetic measurements at temperature above 413 K showed little catalysts deactivation. The reaction rate equations determined in our work are similar to propylene epoxidation using Au/TS-1 catalysts.

■ ASSOCIATED CONTENT

Supporting Information

The Supporting Information is available free of charge on the ACS Publications website at DOI: 10.1021/acs.jpcc.7b10902.

Additional details on SEM images, BET measurements, XANES spectra, EXAFS data fitting, and catalytic performance (PDF)

■ AUTHOR INFORMATION

Corresponding Author

*Phone: 1-256-824-6527. E-mail: yu.lei@uah.edu.

ORCID

C. Heath Turner: 0000-0002-5707-9480

Zili Wu: 0000-0002-4468-3240

Yu Lei: 0000-0002-4161-5568

Notes

The authors declare no competing financial interest.

■ ACKNOWLEDGMENTS

This work is sponsored by the National Science Foundation (Grants CBET-1511820 and CBET-1510485). The authors thank Johnny Goodwin of University of Alabama for taking the STEM images. Part of the work including the BET surface area measurements and UV−vis spectroscopy was conducted at the Center for Nanophase Materials Sciences, which is a DOE Office of Science User Facility. MRCAT operations are supported by the Department of Energy and the MRCAT member institutions. This research used resources of the Advanced Photon Source, a U.S. Department of Energy (DOE) Office of Science User Facility operated for the DOE Office of Science by Argonne National Laboratory under Contract DE-AC02-06CH11357.

■ REFERENCES

(1) Weissermel, K.; Arpe, H.-J. *Industrial Organic Chemistry*, 4th ed.; Wiley-VCH: Weinheim, Germany, 2003.

(2) Hayashi, T.; Tanaka, K.; Haruta, M. Selective Vapor-Phase Epoxidation of Propylene over Au/TiO_2 Catalysts in the Presence of Oxygen and Hydrogen. *J. Catal.* **1998**, *178*, 566−575.

(3) Lei, Y.; Mehmood, F.; Lee, S.; Greeley, J.; Lee, B.; Seifert, S.; Winans, R. E.; Elam, J. W.; Meyer, R. J.; Redfern, P. C.; et al. Increased Silver Activity for Direct Propylene Epoxidation via Subnanometer Size Effects. *Science* **2010**, *328*, 224−228.

(4) Marimuthu, A.; Zhang, J.; Linic, S. Tuning Selectivity in Propylene Epoxidation by Plasmon Mediated Photo-Switching of Cu Oxidation State. *Science* **2013**, *339*, 1590−1593.

(5) Khatib, S. J.; Oyama, S. T. Direct Oxidation of Propylene to Propylene Oxide with Molecular Oxygen: A Review. *Catal. Rev.: Sci. Eng.* **2015**, *57*, 306−344.

(6) Nijhuis, T. A.; Makkee, M.; Moulijn, J. A.; Weckhuysen, B. M. The Production of Propene Oxide: Catalytic Processes and Recent Developments. *Ind. Eng. Chem. Res.* **2006**, *45*, 3447−3459.

(7) Lee, W.-S.; Akatay, M. C.; Stach, E. A.; Ribeiro, F. H.; Delgass, W. N. Gas-Phase Epoxidation of Propylene in the Presence of H_2 and O_2 over Small Gold Ensembles in Uncalcined TS-1. *J. Catal.* **2014**, *313*, 104−112.

(8) Uphade, B. S.; Yamada, Y.; Akita, T.; Nakamura, T.; Haruta, M. Synthesis and Characterization of Ti-MCM-41 and Vapor-Phase Epoxidation of Propylene using H_2 and O_2 over Au/Ti-MCM-41. *Appl. Catal., A* **2001**, *215*, 137−148.

(9) Uphade, B. S.; Akita, T.; Nakamura, T.; Haruta, M. Vapor-Phase Epoxidation of Propene using H_2 and O_2 over Au/Ti-MCM-48. *J. Catal.* **2002**, *209*, 331−340.

(10) Gaudet, J.; Bando, K. K.; Song, Z.; Fujitani, T.; Zhang, W.; Su, D. S.; Oyama, S. T. Effect of Gold Oxidation State on the Epoxidation and Hydrogenation of Propylene on Au/TS-1. *J. Catal.* **2011**, *280*, 40−49.

(11) Huang, J. H.; Lima, E.; Akita, T.; Guzman, A.; Qi, C. X.; Takei, T.; Haruta, M. Propene Epoxidation with O_2 and H_2: Identification of the Most Active Gold Clusters. *J. Catal.* **2011**, *278*, 8−15.

(12) Ferrandez, D. M. P.; Fernandez, I. H.; Teley, M. P. G.; de Croon, M.; Schouten, J. C.; Nijhuis, T. A. Kinetic Study of the Selective Oxidation of Propene with O_2 over Au-Ti Catalysts in the Presence of Water. *J. Catal.* **2015**, *330*, 396−405.

(13) Feng, X.; Sheng, N.; Liu, Y. B.; Chen, X. B.; Chen, D.; Yang, C. H.; Zhou, X. G. Simultaneously Enhanced Stability and Selectivity for Propene Epoxidation with H_2 and O_2 on Au Catalysts Supported on Nano-Crystalline Mesoporous TS-1. *ACS Catal.* **2017**, *7*, 2668−2675.

(14) Sun, Y. N.; Qin, Z. H.; Lewandowski, M.; Carrasco, E.; Sterrer, M.; Shaikhutdinov, S.; Freund, H. J. Monolayer Iron Oxide Film on Platinum Promotes Low Temperature CO Oxidation. *J. Catal.* **2009**, *266*, 359−368.

(15) Fu, Q.; Li, W. X.; Yao, Y. X.; Liu, H. Y.; Su, H. Y.; Ma, D.; Gu, X. K.; Chen, L. M.; Wang, Z.; Zhang, H.; et al. Interface-Confined Ferrous Centers for Catalytic Oxidation. *Science* **2010**, *328*, 1141−1144.

(16) Rodriguez, J. A.; Ma, S.; Liu, P.; Hrbek, J.; Evans, J.; Perez, M. Activity of CeO_x and TiO_x Nanoparticles Grown on Au(111) in the Water-Gas Shift Reaction. *Science* **2007**, *318*, 1757−1760.

(17) Giordano, L.; Pacchioni, G.; Goniakowski, J.; Nilius, N.; Rienks, E. D. L.; Freund, H. J. Charging of Metal Adatoms on Ultrathin Oxide Films: Au and Pd on FeO/Pt(111). *Phys. Rev. Lett.* **2008**, *101*, 026102.

(18) Kulawik, M.; Nilius, N.; Rust, H. P.; Freund, H. J. Atomic Structure of Antiphase Domain Boundaries of a Thin Al_2O_3 Film on NiAl(110). *Phys. Rev. Lett.* **2003**, *91*, 256101.

(19) Sterrer, M.; Risse, T.; Pozzoni, U. M.; Giordano, L.; Heyde, M.; Rust, H. P.; Pacchioni, G.; Freund, H. J. Control of the Charge State of Metal Atoms on Thin MgO Films. *Phys. Rev. Lett.* **2007**, *98*, 096107.

(20) Senanayake, S. D.; Stacchiola, D.; Rodriguez, J. A. Unique Properties of Ceria Nanoparticles Supported on Metal: Novel Inverse Ceria/Copper Catalysts for CO Oxidation and the Water-Gas Shift Reaction. *Acc. Chem. Res.* **2013**, *46*, 1702−1711.

DOI: 10.1021/acs.jpcc.7b10902
J. Phys. Chem. C 2018, 122, 1688−1698

(21) Cabrera, N.; Mott, N. F. Theory of the Oxidation of Metals. *Rep. Prog. Phys.* **1949**, *12*, 163−184.
(22) George, S. M. Atomic Layer Deposition: An Overview. *Chem. Rev.* **2010**, *110*, 111−131.
(23) Zaera, F. The Surface Chemistry of Atomic Layer Depositions of Solid Thin Films. *J. Phys. Chem. Lett.* **2012**, *3*, 1301−1309.
(24) Singh, J. A.; Yang, N.; Bent, S. F. Nanoengineering Heterogeneous Catalysts by Atomic Layer Deposition. *Annu. Rev. Chem. Biomol. Eng.* **2017**, *8*, 41−62.
(25) Lu, J.; Elam, J. W.; Stair, P. C. Atomic Layer Deposition-Sequential Self-Limiting Surface Reactions for Advanced Catalyst "Bottom-Up" Synthesis. *Surf. Sci. Rep.* **2016**, *71*, 410−472.
(26) Ma, L.; Nuwayhid, R. B.; Wu, T.; Lei, Y.; Amine, K.; Lu, J. Atomic Layer Deposition for Lithium-Based Batteries. *Adv. Mater. Interfaces* **2016**, *3*, 1600564.
(27) O'Neill, B. J.; Jackson, D. H. K.; Lee, J.; Canlas, C.; Stair, P. C.; Marshall, C. L.; Elam, J. W.; Kuech, T. F.; Dumesic, J. A.; Huber, G. W. Catalyst Design with Atomic Layer Deposition. *ACS Catal.* **2015**, *5*, 1804−1825.
(28) Piernavieja-Hermida, M.; Lu, Z.; White, A.; Low, K.-B.; Wu, T.; Elam, J. W.; Wu, Z.; Lei, Y. Towards ALD Thin Film Stabilized Single-Atom Pd_1 Catalysts. *Nanoscale* **2016**, *8*, 15348−15356.
(29) Sun, S.; Zhang, G.; Gauquelin, N.; Chen, N.; Zhou, J.; Yang, S.; Chen, W.; Meng, X.; Geng, D.; Banis, M. N.; et al. Single-Atom Catalysis Using Pt/Graphene Achieved through Atomic Layer Deposition. *Sci. Rep.* **2013**, *3*, 1775.
(30) Lei, Y.; Lee, S.; Low, K.-B.; Marshall, C. L.; Elam, J. W. Combining Electronic and Geometric Effects of ZnO-Promoted Pt Nanocatalysts for Aqueous Phase Reforming of 1-Propanol. *ACS Catal.* **2016**, *6*, 3457−3460.
(31) Lu, J. L.; Fu, B. S.; Kung, M. C.; Xiao, G. M.; Elam, J. W.; Kung, H. H.; Stair, P. C. Coking- and Sintering-Resistant Palladium Catalysts Achieved through Atomic Layer Deposition. *Science* **2012**, *335*, 1205−1208.
(32) Onn, T. M.; Zhang, S. Y.; Arroyo-Ramirez, L.; Chung, Y. C.; Graham, G. W.; Pan, X. Q.; Gorte, R. J. Improved Thermal Stability and Methane-Oxidation Activity of Pd/Al_2O_3 Catalysts by Atomic Layer Deposition of ZrO_2. *ACS Catal.* **2015**, *5*, 5696−5701.
(33) Gould, T. D.; Lubers, A. M.; Corpuz, A. R.; Weimer, A. W.; Falconer, J. L.; Medlin, J. W. Controlling Nanoscale Properties of Supported Platinum Catalysts through Atomic Layer Deposition. *ACS Catal.* **2015**, *5*, 1344−1352.
(34) Lei, Y.; Liu, B.; Lu, J. L.; Lobo-Lapidus, R. J.; Wu, T. P.; Feng, H.; Xia, X. X.; Mane, A. U.; Libera, J. A.; Greeley, J. P.; et al. Synthesis of Pt-Pd Core-Shell Nanostructures by Atomic Layer Deposition: Application in Propane Oxidative Dehydrogenation to Propylene. *Chem. Mater.* **2012**, *24*, 3525−3533.
(35) Wang, X. F.; Zhao, H. Y.; Wu, T. P.; Liu, Y. Z.; Liang, X. H. Synthesis of Highly Dispersed and Highly Stable Supported Au-Pt Bimetallic Catalysts by a Two-Step Method. *Catal. Lett.* **2016**, *146*, 2606−2613.
(36) Cao, K.; Liu, X.; Zhu, Q. Q.; Shan, B.; Chen, R. Atomically Controllable Pd@Pt Core-Shell Nanoparticles towards Preferential Oxidation of CO in Hydrogen Reactions Modulated by Platinum Shell Thickness. *ChemCatChem* **2016**, *8*, 326−330.
(37) Wu, Y.; Lu, Z.; Emdadi, L.; Oh, S. C.; Wang, J.; Lei, Y.; Chen, H.; Tran, D. T.; Lee, I. C.; Liu, D. Tuning External Surface of Unit-Cell Thick Pillared MFI and MWW Zeolites by Atomic Layer Deposition and its Consequences on Acid-Catalyzed Reactions. *J. Catal.* **2016**, *337*, 177−187.
(38) Xu, D.; Wu, B. S.; Ren, P. J.; Wang, S. Y.; Huo, C. F.; Zhang, B.; Guo, W. P.; Huang, L. H.; Wen, X. D.; Qin, Y.; et al. Controllable Deposition of Pt Nanoparticles into a KL Zeolite by Atomic Layer Deposition for Highly Efficient Reforming of n-heptane to Aromatics. *Catal. Sci. Technol.* **2017**, *7*, 1342−1350.
(39) Gong, T.; Qin, L. J.; Lu, J.; Feng, H. ZnO Modified ZSM-5 and Y Zeolites Fabricated by Atomic Layer Deposition for Propane Conversion. *Phys. Chem. Chem. Phys.* **2016**, *18*, 601−614.
(40) Ritala, M.; Leskela, M.; Niinisto, L.; Haussalo, P. Titanium Isopropoxide as a Precursor in Atomic Layer Epitaxy of Titanium Dioxide Thin Films. *Chem. Mater.* **1993**, *5*, 1174−1181.
(41) Wu, Z. L.; Zhou, S. H.; Zhu, H. G.; Dai, S.; Overbury, S. H. DRIFTS-QMS Study of Room Temperature CO Oxidation on Au/SiO_2 Catalyst: Nature and Role of Different Au Species. *J. Phys. Chem. C* **2009**, *113*, 3726−3734.
(42) Lei, Y.; Liu, B.; Lu, J.; Libera, J. A.; Greeley, J. P.; Elam, J. W. Effects of Chlorine in Titanium Oxide on Palladium Atomic Layer Deposition. *J. Phys. Chem. C* **2014**, *118*, 22611−22619.
(43) Almeida, R. M.; Pantano, C. G. Structural Investigation of Silica-Gel Films by Infrared-Spectroscopy. *J. Appl. Phys.* **1990**, *68*, 4225−4232.
(44) Kim, Y. H.; Hwang, M. S.; Kim, H. J.; Kim, J. Y.; Lee, Y. Infrared Spectroscopy Study of Low-Dielectric-Constant Fluorine-Incorporated and Carbon-Incorporated Silicon Oxide Films. *J. Appl. Phys.* **2001**, *90*, 3367−3370.
(45) Lei, Y.; Zhao, H. Y.; Diaz-Rivas, R.; Lee, S.; Liu, B.; Lu, J. L.; Stach, E. A.; Winans, R. E.; Chapman, K. W.; Greeley, J. P.; et al. Adsorbate-Induced Structural Changes in 1−3 nm Platinum Nanoparticles. *J. Am. Chem. Soc.* **2014**, *136*, 9320−9326.
(46) Lei, Y.; Jelic, J.; Nitsche, L. C.; Meyer, R.; Miller, J. T. Effect of Particle Size and Adsorbates on the L_3, L_2 and L_1 X-ray Absorption Near Edge Structure of Supported Pt Nanoparticles. *Top. Catal.* **2011**, *54*, 334−348.
(47) Miller, J. T.; Kropf, A. J.; Zha, Y.; Regalbuto, J. R.; Delannoy, L.; Louis, C.; Bus, E.; van Bokhoven, J. A. The Effect of Gold Particle Size on Au-Au Bond Length and Reactivity toward Oxygen in Supported Catalysts. *J. Catal.* **2006**, *240*, 222−234.
(48) Nijhuis, T. A.; Sacaliuc-Parvulescu, E.; Govender, N. S.; Schouten, J. C.; Weckhuysen, B. M. The Role of Support Oxygen in the Epoxidation of Propene over Gold-Titania Catalysts Investigated by Isotopic Transient Kinetics. *J. Catal.* **2009**, *265*, 161−169.
(49) Biener, J.; Farfan-Arribas, E.; Biener, M.; Friend, C. M.; Madix, R. J. Synthesis of TiO_2 Nanoparticles on the Au(111) Surface. *J. Chem. Phys.* **2005**, *123*, 094705.
(50) Brown, M. A.; Fujimori, Y.; Ringleb, F.; Shao, X.; Stavale, F.; Nilius, N.; Sterrer, M.; Freund, H. J. Oxidation of Au by Surface OH: Nucleation and Electronic Structure of Gold on Hydroxylated MgO(001). *J. Am. Chem. Soc.* **2011**, *133*, 10668−10676.
(51) Wang, C.; Wang, H.; Yao, Q.; Yan, H.; Li, J.; Lu, J. Precisely Applying TiO_2 Overcoat on Supported Au Catalysts Using Atomic Layer Deposition for Understanding the Reaction Mechanism and Improved Activity in CO Oxidation. *J. Phys. Chem. C* **2016**, *120*, 478−486.
(52) Sinha, A. K.; Seelan, S.; Akita, T.; Tsubota, S.; Haruta, M. Vapor Phase Propylene Epoxidation over Au/Ti-MCM-41 Catalysts Prepared by Different Ti Incorporation Modes. *Appl. Catal., A* **2003**, *240*, 243−252.
(53) Sinha, A. K.; Seelan, S.; Okumura, M.; Akita, T.; Tsubota, S.; Haruta, M. Three-Dimensional Mesoporous Titanosilicates Prepared by Modified Sol-Gel Method: Ideal Gold Catalyst Supports for Enhanced Propene Epoxidation. *J. Phys. Chem. B* **2005**, *109*, 3956−3965.
(54) Yap, N.; Andres, R. P.; Delgass, W. N. Reactivity and Stability of Au in and on TS-1 for Epoxidation of Propylene with H_2 and O_2. *J. Catal.* **2004**, *226*, 156−170.
(55) Tsukamoto, D.; Shiraishi, Y.; Sugano, Y.; Ichikawa, S.; Tanaka, S.; Hirai, T. Gold Nanoparticles Located at the Interface of Anatase/Rutile TiO_2 Particles as Active Plasmonic Photocatalysts for Aerobic Oxidation. *J. Am. Chem. Soc.* **2012**, *134*, 6309−6315.
(56) Nijhuis, T. A.; Visser, T.; Weckhuysen, B. M. Mechanistic Study into the Direct Epoxidation of Propene over Gold/Titania Catalysts. *J. Phys. Chem. B* **2005**, *109*, 19309−19319.
(57) Mul, G.; Zwijnenburg, A.; van der Linden, B.; Makkee, M.; Moulijn, J. A. Stability and Selectivity of Au/TiO_2 and Au/TiO_2/SiO_2 Catalysts in Propene poxidation: An in situ FT-IR study. *J. Catal.* **2001**, *201*, 128−137.

DOI: 10.1021/acs.jpcc.7b10902
J. Phys. Chem. C 2018, 122, 1688−1698

(58) Bravo-Suarez, J. J.; Bando, K. K.; Lu, J.; Haruta, M.; Fujitani, T.; Oyama, S. T. Transient Technique for Identification of True Reaction Intermediates: Hydroperoxide Species in Propylene Epoxidation on Gold/Titanosilicate Catalysts by X-ray Absorption Fine Structure Spectroscopy. *J. Phys. Chem. C* **2008**, *112*, 1115−1123.
(59) Nijhuis, T. A.; Huizinga, B. J.; Makkee, M.; Moulijn, J. A. Direct Epoxidation of Propene Using Gold Dispersed on TS-1 and Other Titanium-Containing Supports. *Ind. Eng. Chem. Res.* **1999**, *38*, 884−891.
(60) Taylor, B.; Lauterbach, J.; Blau, G. E.; Delgass, W. N. Reaction Kinetic Analysis of the Gas-Phase Epoxidation of Propylene over Au/TS-1. *J. Catal.* **2006**, *242*, 142−152.
(61) Sinha, A.; Seelan, S.; Tsubota, S.; Haruta, M. Catalysis by Gold Nanoparticles: Epoxidation of Propene. *Top. Catal.* **2004**, *29*, 95−102.
(62) Taylor, B.; Lauterbach, J.; Delgass, W. N. Gas-Phase Epoxidation of Propylene over Small Gold Ensembles on TS-1. *Appl. Catal., A* **2005**, *291*, 188−198.

DOI: 10.1021/acs.jpcc.7b10902
J. Phys. Chem. C 2018, 122, 1688−1698